Journal of Materials Chemistry A

ROYAL SOCIETY OF CHEMISTRY

PAPER

View Article Online
View Journal | View Issue

Cite this: J. Mater. Chem. A, 2025, 13, 17709

Failure of protonic ceramic fuel cells (PCFCs) under gaseous Cr and CO_2 exposure and the introduction of a protective barrier layer for mitigation†

Yeji Lim,‡[ab] Jong Heon Chong,‡[ac] Puspendu Guha,[a] Wan-Jae Lee,[ad] Inhyeok Cho,[e] Seol Hee Oh,[a] Junseok Kim,[ab] Kyung Joong Yoon,[a] Ji-Won Son,[ac] Jong-Ho Lee,[ad] Sihyuk Choi,[e] Deok-Hwang Kwon,[a] Ho-Il Ji *[ad] and Sungeun Yang *[ad]

Received 19th September 2024
Accepted 30th April 2025

DOI: 10.1039/d4ta06672c

rsc.li/materials-a

Protonic ceramic fuel cells (PCFCs) are attracting widespread interest due to their high efficiency and relatively low operating temperatures. However, the stability of PCFCs under realistic operating conditions, which include exposure to volatile Cr species and CO_2 in the air electrode compartment, has rarely been examined. Here, we test a PCFC composed of $BaCe_{0.4}Zr_{0.4}Y_{0.1}Yb_{0.1}O_{3-\delta}$ as the electrolyte and $PrBa_{0.5}Sr_{0.5}Co_{1.5}Fe_{0.5}O_{5+\delta}$ as the air electrode, with a metallic interconnect and atmospheric air as an oxidant gas. The complete phase decomposition of the electrolyte and the formation of $BaCO_3$ at the air electrode/electrolyte interface were observed after sudden cell failure within 20 hours of operation. Detailed analyses and control tests confirm the effects of Cr and CO_2 species on cell degradation. In contrast, the PBSCF air electrode remains relatively stable. We also report on the effectiveness of applying a thin and dense PBSCF protective barrier layer between the electrolyte and the air electrode, which significantly improves stability under realistic operating conditions.

1. Introduction

Protonic ceramic fuel cells (PCFCs) are a subset of solid oxide fuel cells (SOFCs) that operate in the lower temperature range of 400–600 °C, conducting protons (H^+) instead of oxide ions (O^{2-}). The operating temperature range of PCFCs is high enough to retain the advantages of conventional SOFCs, such as high efficiency, fuel flexibility, and the use of low-cost catalysts. Conversely, it is also low enough to allow for the utilization of low-cost metallic interconnects, faster start-up, and improved stability. Recent research efforts in PCFCs have achieved substantial performance improvements through the development of electrolyte materials[1–3] and air electrode materials,[4–11] as well as cell processing methods to reduce high sintering temperatures.[12–17] In the past decade, the potential of PCFCs has been demonstrated by operating at 450 °C,[18,19] scaling up to 25 cm^2,[13] and achieving efficient fuel flexible,[20] and reversible operation.[6,11,21,22]

Most research reports the performance of PCFCs in ideal environments, utilizing ceramic jigs and high-purity gases. However, the cells can suffer significantly under realistic operating conditions involving Cr-containing metallic interconnects and atmospheric air as an oxidant gas. Volatile Cr species, $CrO_2(OH)_2$ and CrO_3, form from the metallic interconnects during the operation of PCFCs and SOFCs.[23–25] These Cr species and CO_2, which are acidic, can easily react with alkaline earth metal cations such as Ba and Sr. PCFCs may suffer more severely than SOFCs for two main reasons. First, barium oxide—the most widely used constituent of proton-conducting oxides—has one of the strongest tendencies to form metal chromate ($MCrO_4$) and metal carbonate (MCO_3).[26,27] Second, the vapor pressure of gaseous Cr species and the resulting Cr poisoning increased with an increasing partial pressure of H_2O, where the presence of H_2O is inevitable in the air electrode compartment during PCFC operation.[24,28,29]

Although PCFCs are expected to suffer severely under realistic operating conditions, there are only a few studies addressing this issue. Zhao *et al.* studied the reaction between volatile Cr species and $BaZr_{0.1}Ce_{0.7}Y_{0.2}O_{3-\delta}$ at temperatures between 600 and 800 °C. Cr deposition on the surface of $BaZr_{0.1}Ce_{0.7}Y_{0.2}O_{3-\delta}$ led to decreased conductivity.[30] Le *et al.* tested a PCFC in a fuel cell stack with a Crofer 22H interconnect

[a]Center for Energy Materials Research, Korea Institute of Science and Technology (KIST), Seoul 02792, Republic of Korea. E-mail: hiji@kist.re.kr; syang@kist.re.kr
[b]Department of Materials Science and Engineering, Korea University, Seoul 02841, Republic of Korea
[c]Graduate School of Energy and Environment (KU-KIST Green School), Korea University, Seoul 02841, Republic of Korea
[d]Division of Nanoscience & Technology, Korea University of Science and Technology (UST), KIST Campus, Seoul 02792, Republic of Korea
[e]Department of Mechanical Engineering, Kumoh National Institute of Technology, Gumi, Gyeongbuk 39177, Republic of Korea

† Electronic supplementary information (ESI) available. See DOI: https://doi.org/10.1039/d4ta06672c

‡ These authors contributed equally to this work.

and reported significant performance degradation. The degradation was alleviated by applying a GDC interlayer between the electrolyte and the air electrode, although the reason remained unclear, and synthetic air was used instead of atmospheric air.[31] Zhang *et al.* focused on the stability of the air electrode $PrBa_{0.5}Sr_{0.5}Co_{1.5}Fe_{0.5}O_{5+\delta}$ (PBSCF), and reported Cr poisoning in the presence of a Crofer 22 APU sheet with humidified air. Infiltration of $Pr_{0.9}Fe_{0.7}Co_{0.3}O_3$ into the porous cathode layer with a PBSCF cathode and BCZYYb7111 electrolyte improved the Cr poisoning-related degradation.[32]

In this work, we analyze the degradation behavior of PCFCs under realistic operating conditions that employ metallic interconnects and atmospheric air. For the first time, the degradation mechanism of a PCFC was studied in detail using SEM, XRD, STEM-EDS, and SAED analyses, accompanied by control tests. Based on these analyses, we propose a degradation mechanism for PCFCs under realistic operating conditions. To improve the long-term stability of the cell, we introduce the concept of a protective barrier layer, which physically shields the electrolyte from exposure to gaseous Cr species and CO_2.

2. Materials and methods

2.1. Cell fabrication

A protonic ceramic fuel cell was fabricated using pelletizing and screen-printing techniques. The cell had a circular design with an anode support diameter of 22.5 mm and a cathode diameter of 10 mm. Raw materials for the fuel electrode support layer included NiO (Mechema, Taiwan) and $BaCe_{0.4}Zr_{0.4}Y_{0.1}Yb_{0.1}O_{3-\delta}$ (BCZYYb4411) powder (Kceracell, Korea), along with a poly(-methyl methacrylate) pore-forming agent (Sunjin Beauty Science, Korea). NiO and BCZYYb4411 powders were ball-milled for 100 h to achieve uniform particle size. NiO powder, BCZYYb4411 powder, and PMMA, in a volumetric ratio of 32 : 32 : 36, were further ball-milled for 24 h with zirconia balls. The resulting powder was then pelletized at 50 MPa using a 30 mm-diameter round mold, resulting in a 1.3 mm thick pellet serving as the anode support layer. After pre-sintering the support layer at 950 °C, the fuel electrode functional layer and electrolyte were layered using a screen-printing process. The fabricated half-cell was co-sintered at 1400 °C for 4 h. The air electrode paste was screen-printed onto the sintered half-cell electrolyte. The final sintering step at 950 °C for 5 h completed the full cell structure: NiO-BCZYYb4411/BCZYYb4411/PBSCF. For the fuel electrode functional layer, electrolyte, and air electrode functional layer pastes, NiO, NiO and BCZYYb4411, or $PrBa_{0.5}Sr_{0.5}Co_{1.5}Fe_{0.5}O_{5+\delta}$ (PBSCF) powders were mixed with α-terpineol (Daejung Chemicals & Metals, Korea), dispersant (KD-6, Croda, United Kingdom), binder (BH3, Sekisui Chemical, Japan), and plasticizer (DBP, Junsei, Japan), followed by 48 h of milling using a planetary milling machine.

2.2. Protective barrier layer fabrication

A dense interlayer between the electrolyte and air electrode was prepared using pulsed laser deposition. The dense PBSCF interlayer was deposited onto the electrolyte of the sintered half-cell, which included the anode support, anode functional layer, and electrolyte. The deposition of the dense PBSCF interlayer occurred at 650 °C in an oxygen atmosphere at 4.00 Pa (30 mTorr). The interlayer thickness was controlled by varying the deposition time. The cell was then finalized by forming a porous air electrode through screen printing the air electrode paste onto the PBSCF dense layer, followed by final sintering at 950 °C for 5 h.

2.3. Fuel cell tests

The fabricated cell (NiO-BCZYYb4411/BCZYYb4411/PBSCF) underwent electrochemical cell testing using a lab-made test station. Ni foam and gold mesh were used as current collectors for the fuel electrode and air electrode, respectively. A glass sealant was applied to prevent gas leakage. All the components were assembled in an Inconel 600 alloy metal interconnector manifold, and gases were delivered *via* SUS 316L tubing. Wet hydrogen (3% H_2O, 97% H_2) and atmospheric air were introduced to the fuel electrode and air electrode, respectively, with a flow rate of 200 sccm. Atmospheric air was dust filtered and dehydrated before use, but the dehydration was conducted to avoid condensation at room temperature, and therefore, the gas is not fully dry. Electrochemical measurements were conducted using a frequency response analyzer and potentiostat (Solartron 1260/1287, Solartron Analytical, United Kingdom). Electrochemical impedance spectra were acquired with a 20 mV AC amplitude across a frequency range from 10^6 Hz to 10^{-1} Hz at open-circuit voltage.

2.4. Fuel cell test under Cr- and CO_2-free conditions

A comparison test was performed using an alumina jig and N_2/O_2 mixed gas as the air electrode gas supply, ensuring a cleaner testing environment. For an alumina jig test, Ag wires (Goodfellow, United Kingdom) were attached as a current collector at both the anode and cathode sides using Ag paste (SPI supplies). The anode-supported cell was fixed onto the alumina tube and sealed with a ceramic adhesive (Ceramabond 552, Aremco). Humidified hydrogen (3% H_2O, 99.9999% H_2) was supplied to the fuel electrode side with a flow rate of 50 sccm, while dry air (high purity compressed air, 99.999%) was applied to the air electrode side with a flow rate of 150 sccm. All gases were delivered through ceramic tubes at operating temperature without a Cr-containing metallic component.

2.5. Cr and CO_2 exposure tests

For the Cr exposure test, porous pellets of BCZYYb4411, PBSCF, and Cr_2O_3 were prepared for the Cr poisoning test. BCZYYb4411 powder was synthesized by the conventional solid-state reaction method, while commercially available PBSCF (KCeracell, Korea) and Cr_2O_3 (Daejeong, Korea) powders were used for pellet preparation. The pelletized powders, with a diameter of 5 mm and a thickness of 2 mm, were heat-treated at 600 °C for 24 h. In the test setup, the BCZYYb4411 or PBSCF pellet was placed adjacent to the Cr_2O_3 pellet, with Pt mesh placed in between to prevent direct contact, simulating cell operating conditions.

The pellets were exposed to a temperature of 600 °C using either dry N_2/O_2 mixed gas or N_2/O_2 mixed gas with 3% H_2O. For the CO_2 exposure test, BCZYYb4411 and PBSCF powders were heat treated under atmospheric air, containing CO_2, at 600 °C for 24 h.

2.6. Characterization

Crystal structures of powders and fabricated cells were examined by using X-ray diffraction (XRD) with Cu Kα radiation (λ = 1.542 Å) on instruments P1 (Rigaku, Japan), T1 (Rigaku, Japan), or D8 (Bruker, USA). Microstructures of cells were evaluated by scanning electron microscopy (SEM, Inspect F, FEI, Japan). The stability of the electrolyte material under carbon dioxide gas conditions was assessed by thermogravimetric analysis (TGA, SDT Q600, TA Instruments, USA). The samples were heated to 500 °C at a rate of 10 °C min^{-1} under N_2 gas flow and exposed to CO_2 gas flow at 500 °C for 8 h. The stability of air electrode materials under humid conditions was determined using commercial powders, $PrBa_{0.5}Sr_{0.5}Co_{1.5}Fe_{0.5}O_{5+\delta}$ (PBSCF, KCereacell, Republic of Korea), $BaCe_{0.4}Fe_{0.4}Zr_{0.1}Y_{0.1}O_{3-\delta}$ (BCFZY, KCeracell, Republic of Korea), and $Ba_{0.5}Sr_{0.5}Co_{0.8}Fe_{0.2}O_{3-\delta}$ (BSCF, AGC SEIMI Chemical, Japan). The powders were treated with 30% H_2O (balanced with N_2/O_2 mixed gas) at 550 °C for 300 h. Transmission electron microscopy (TEM) specimens were prepared using a focused ion (Ga^+ ions) beam (FIB) system (Helios G4, FEI, USA) with a thickness of ~80 nm. Structural properties with chemical analyses were inspected using a field emission gun (FEG)-based TEM system with a 200 kV acceleration voltage (analytical TEM Talos, F200X, FEI, USA), equipped with four integrated super-X energy-dispersive X-ray spectroscopy (EDS) detectors.

3. Results and discussion

3.1. Failure of PCFCs under realistic operating conditions

We studied PCFCs composed of a Ni–$BaCe_{0.4}Zr_{0.4}Y_{0.1}Yb_{0.1}O_{3-\delta}$ (BCZYYb4411) cermet fuel electrode, a BCZYYb4411 electrolyte, and a PBSCF air electrode (Fig. 1a). We chose the BCZYYb4411 electrolyte instead of $BaCe_{0.7}Zr_{0.1}Y_{0.1}Yb_{0.1}O_{3-\delta}$ (BCZYYb7111) because the 4411 composition is more stable when exposed to CO_2 (Fig. S1†).[4] PBSCF was selected as the air electrode due to its chemical compatibility with the BCZYYb4411 electrolyte[4] and stability in a humid environment compared to its counterparts, $BaCe_{0.4}Fe_{0.4}Zr_{0.1}Y_{0.1}O_{3-\delta}$, and $Ba_{0.5}Sr_{0.5}Co_{0.8}Fe_{0.2}O_{3-\delta}$ (Fig. S2†).

The cell testing environment resembles a single repeating unit of a fuel cell stack, designed to examine the performance and stability of PCFCs under realistic operating conditions. The testing jig was made with an Inconel 600 interconnect with SUS 316L gas tubing (Fig. 1b). Both metals have a Cr_2O_3 surface skin, which can serve as a source of volatile Cr species capable of reacting with and degrading the air electrode and electrolyte. A glass sealant was used to prevent gas leaks, and atmospheric air containing CO_2 and H_2O was used as the oxidant gas.

The cell initially exhibited excellent performance, achieving peak power densities of 1.31, 0.99, and 0.71 W cm^{-2} at 650, 600, and 550 °C, respectively (Fig. 1c), which are comparable to state-of-the-art PCFCs.[2,6,8,15,16,19,33] After testing the cell at three

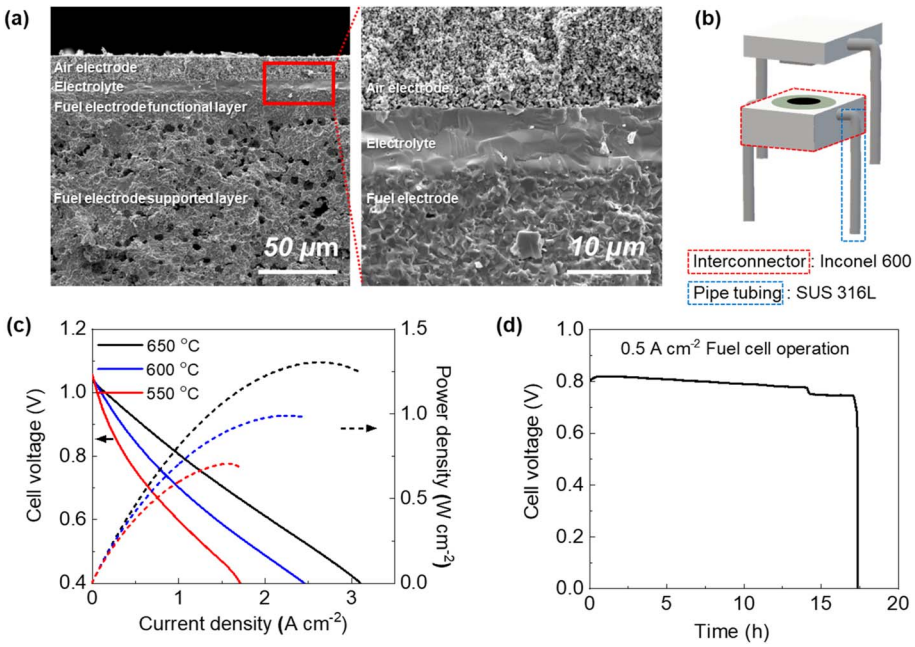

Fig. 1 Initial microstructure and performance testing of the PCFC under realistic operating conditions. (a) Cross-sectional SEM image of the fabricated PCFC, illustrating the layers from bottom to top: fuel electrode, electrolyte, and air electrode. (b) Schematic of the single-cell test set-up used to evaluate PCFC performance. (c) *I–V–P* curves of the cell from 650 °C to 550 °C, using 3% humidified H_2 and atmospheric air as feed gases for the fuel electrode and air electrode, respectively. (d) Galvanostatic test conducted at 600 °C and a current density of 0.5 A cm^{-2} under fuel cell operating conditions.

different temperatures, a galvanostatic stability test was conducted at 600 °C at a current density of 0.5 A cm^{-2}. Unlike its high initial performance, the cell deteriorated rapidly and ceased functioning before reaching 20 hours of operation (Fig. 1d). Following a short initial activation period, the cell degraded at a linear-fitted degradation rate of 428% kh^{-1}. After ~17 hours of operation, sudden potential drops occurred, resulting in complete cell failure. The cell degradation rate is significantly higher than previously reported for PCFCs, which showed negligible degradation over hundreds to thousands of hours.[2,6,8,15,16,19,33]

We tested the same cell without exposure to Cr species and CO_2 (Fig. S3†). The cell was tested using an alumina jig with synthetic air (N_2/O_2 mixed gas). Similar initial performance was observed, and the cell performance slightly degraded over the course of a 20 h test, without experiencing drastic cell failure. The peak power density decreased from 0.90 to 0.79 W cm^{-2}, which is remarkably more stable than the drop from 0.99 to 0.08 W cm^{-2} under realistic operating conditions. Cross-sectional SEM images show no signs of degradation (Fig. S3d and e†). This test confirmed that Cr and/or CO_2 indeed play significant roles in the performance degradation of PCFCs.

Cr and CO_2 exposure tests were conducted on BCZYYb4411 and PBSCF to verify the stability of these materials. For the Cr exposure test, pellets of BCZYYb4411 and PBSCF were placed next to a Cr_2O_3 pellet without physical contact and were treated in both dry and 3% humidified air at 600 °C for 24 h (Fig. S4a and b†). BCZYYb4411 clearly showed the formation of $BaCrO_4$ under humidified air conditions, but no secondary peak was observed under dry air conditions. The presence of water increases the partial pressure of volatile $CrO_2(OH)_2$ species and thus is responsible for the difference between humidified and dry conditions (Fig. S5†).[24] In contrast, PBSCF showed no signs of secondary phase formation under either condition, but a subtle peak shift under wet conditions was noted, suggesting minor Cr-related degradation in PBSCF. For the CO_2 exposure test, powders of BCZYYb4411 and PBSCF were exposed to ambient air, containing CO_2, at 600 °C for 24 h. XRD analysis revealed that both materials remained stable under CO_2 exposure without noticeable changes (Fig. S4c and d†). These results align well with the Gibbs free energy calculations for carbonate and chromate formation from various Ba oxides and Sr oxides (Fig. S6†). The formation of chromates exhibits much more negative Gibbs free energy, indicating that chromates form more readily than carbonates. For example, at 600 °C, the Gibbs free energy of $BaCrO_4$ formation is −310.2 kJ mol^{-1} and −234.4 kJ mol^{-1}, which are significantly more negative the Gibbs free energy for $BaCO_3$ formation, −72.2 kJ mol^{-1} and 3.6 kJ mol^{-1} from $BaCeO_3$ and $BaZrO_3$, respectively. These tests demonstrate that while BCZYYb4411 is prone to Cr-related degradation, it remains stable under exposure to CO_2; PBSCF remained stable under both Cr and CO_2 exposure tests.

To the best of our knowledge, there are two previous studies that report cell degradation with metallic components and under exposure to CO_2.[31,32] Le *et al.* reported a degradation rate of 36% kh^{-1} with a Crofer 22H stainless steel interconnect, which was improved to 3% kh^{-1} by applying a GDC interlayer between the electrolyte and the air electrode, although synthetic air without CO_2 was used in this report.[31] Zhang *et al.* reported a degradation rate of 120% kh^{-1} with a Crofer 22 APU stainless steel sheet placed adjacent to the cathode, which was improved to 20% kh^{-1} by infiltration of stable $Pr_{0.9}Fe_{0.7}Co_{0.3}O_3$ to the porous cathode layer with the PBSCF cathode and BCZYYb7111 electrolyte.[32] These improved rates are still higher than the industrial target of 0.114–0.228% kh^{-1}, which aims 10% degradation over 5–10 years of operation. We have conducted SEM, XRD, STEM-EDS, and SAED studies to examine and understand the origin of the low stability in our PCFC testing.

3.2. Post-mortem analysis of the failed PCFC

Post-mortem analysis of the failed cell was conducted to study its degradation behavior. SEM images of the degraded cell were compared with those of the as-prepared cell (Fig. 2a–f). The surface of the bare electrolyte (electrolyte region without a covered air electrode) exhibited the formation of a secondary phase attributed to $BaCrO_4$, later confirmed by XRD analysis (Fig. 2a and d). The morphology of PBSCF also underwent noticeable changes, appearing more edged (Fig. 2b and e). Cross-sectional SEM images revealed more drastic changes (Fig. 2c and f). The initially dense electrolyte became porous-like, undergoing complete deformation throughout its thickness, and a secondary phase was observed at the air electrode/electrolyte interface.

Additional SEM images (Fig. S7a and b†) revealed partial degradation starting at the PBSCF/BCZYYb4411 interface. It is worth mentioning that the bare electrolyte region without a covered air electrode did not exhibit the same type of phase decomposition and still retained a dense electrolyte structure with weakened grain boundaries after the cell test (Fig. S7c and d†). Although we observed the formation of $BaCrO_4$ at the surface of the bare electrolyte, this alone did not lead to substantial electrolyte degradation. We assume that the electrochemical reactions occurring at the air electrode/electrolyte interface, or the interplay between the air electrode and electrolyte materials, could be the causes of this difference.

XRD analysis of the surface of the bare electrolyte and the air electrode-covered region was conducted using grazing incident XRD and compared with the initial powders (Fig. 2g, h, and S8† for more details). Both the bare BCZYYb4411 and PBSCF-covered regions exhibited phase decomposition after the cell test. The majority of BCZYYb4411 retained its crystalline structure with a small amount of secondary phases, including $BaCrO_4$ and Y_2O_3 (or Yb_2O_3). More severe phase decomposition was observed on the surface of the air electrode-covered region. Crystalline phases of both PBSCF and BCZYYb4411 were observed, indicating that the XRD data contained information not only from the air electrode but also from the interface and the electrolyte. Similar to the bare electrolyte region, $BaCrO_4$ was observed, along with a secondary perovskite phase that could be identified as $Sr_{0.5}Ba_{0.5}CoO_{2.5}$ or $BaFeO_3$. A small peak at 23.9° could potentially be assigned to $BaCO_3$. The XRD results, consistent with SEM images, indicate severe phase decomposition in the air electrode-covered electrolyte region

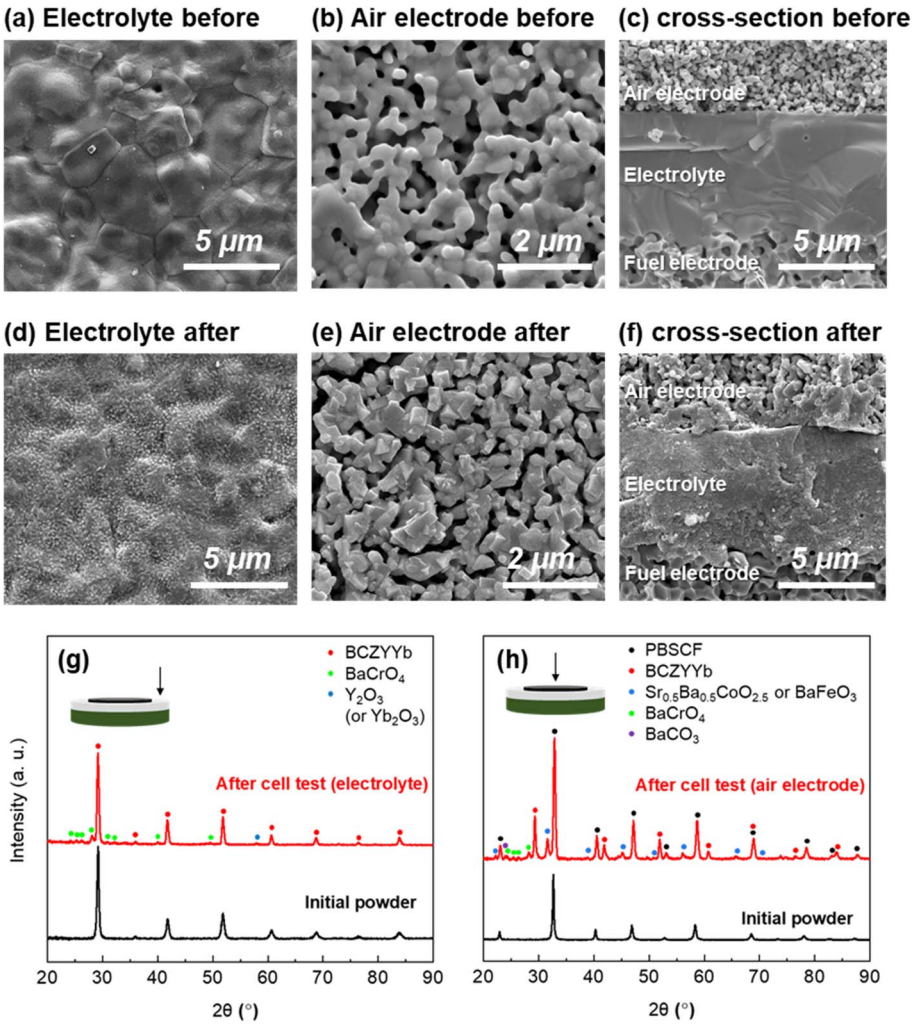

Fig. 2 SEM and XRD analyses of the PCFC before and after the 20 h cell test. (a–c) SEM images of the BCZYYb4411 electrolyte, PBSCF air electrode, and cross-sectional view of the cell before the cell test. (d–f) SEM images of the BCZYYb4411 electrolyte, PBSCF air electrode, and cross-sectional view of the cell after the 20 h cell test. X-ray diffraction patterns of the (g) BCZYYb4411 electrolyte and (h) PBSCF air electrode after the cell test compared to the corresponding initial powders. See Fig. S8† for more details.

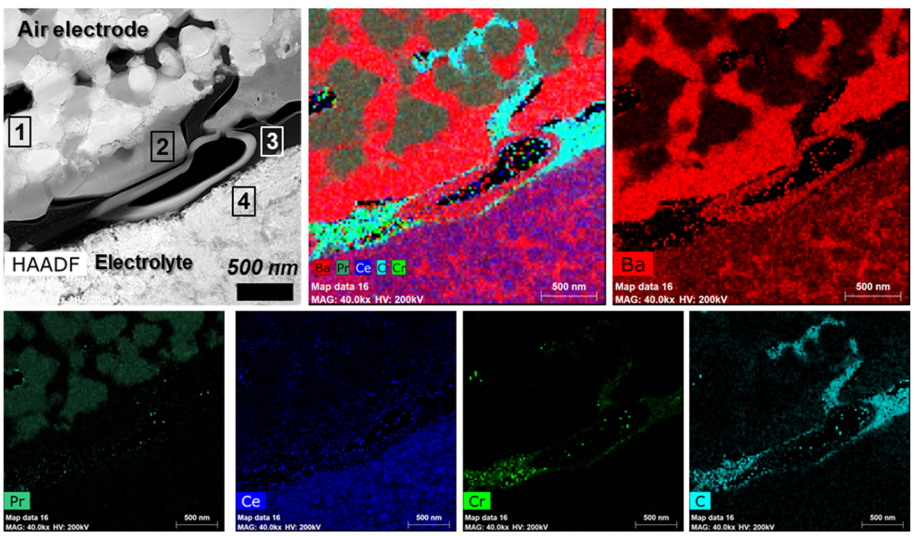

Fig. 3 Detailed investigation of degradation at the air electrode/electrolyte interface after the 20 h cell test. HAADF-STEM image alongside EDS mapping images of the constituent elements, Ba, Pr, Ce, Cr, and C. Quantitative elemental mapping was applied for all the elements.

Table 1 Cation composition analysis from EDS in Fig. 3. Carbon has been excluded from the analysis because the resin used in sample preparation contains carbon

Region	Concentration [at%] (stoichiometric value [at%])					
(1) PBSCF air electrode	Pr	Ba	Sr	Co	Fe	Cr
	22.4 (25)	12.2 (12.5)	18.1 (12.5)	33.2 (37.5)	13.6 (12.5)	—
(2) New phase	Ba	Ce	Zr	Y	Yb	Cr
	85.0	4.9	5.3	1.0	2.7	1.1
(3) Gap	Cr: 100					
(4) BCZYYb4411 electrolyte	Ba	Ce	Zr	Y	Yb	Cr
	30.7 (50)	20.0 (20)	29.4 (20)	6.5 (5)	11.8 (5)	1.6

after the cell test. However, due to the small and overlapping peaks, definitive assignment was challenging.

3.3. HR-TEM analysis of the failed PCFC

HR-TEM analysis was conducted to study the phase decomposition behavior at the interface in detail. STEM-EDS and SAED were employed to investigate the compositions and the decomposed phases. EDS mapping images are presented in Fig. 3, with cation compositions at distinct positions (boxed numbers) shown in Table 1. Notably, significant variations in Ba concentration were observed, associated with variations in C and Cr, with entirely different behaviors across the air electrode, electrolyte and interface regions.

At the air electrode, PBSCF particles mostly retained their shape and composition (Position 1 in Fig. 3), as well represented in the Pr map, indicating that the PBSCF at the interface remained intact. However, the edges of the particles were observed to be slightly fragmented, which could result from degradation starting from the surface. At the interface between the air electrode and electrolyte, a newly formed Ba-rich phase is observed (Position 2 in Fig. 3), also seen in SEM images (Fig. 2f). Interestingly, this Ba-rich phase is associated with a slight increase in intensity in the C map, along with a small amount of Cr. This new phase was observed at the interface and filled up the pores of the air electrode. Delamination was noted at the interface (Position 3 in Fig. 3), characterized predominantly by the presence of Cr. At the electrolyte, severe phase decompositions were evident (Position 4 in Fig. 3). The Ba map showed drastic composition changes, and Ce elements were separated disproportionately with Ba (see also Fig. S9†). The cation composition analysis revealed that the decomposed electrolyte is significantly Ba-deficient from its initial composition, decreasing from 50% to 30.7%. In addition, neither Au, Si, nor Al—elements of the current collector and sealant used in testing—were detected above the detection limit, suggesting a minimal effect of these species on the observed cell degradation.

To better identify the decomposed phases, we investigated SAED patterns across distinctive areas. Surprisingly, SAED of the interface between the air electrode and electrolyte demonstrated the presence of large $BaCO_3$ crystalline phases (Fig. 4c; compare with the simulated SAED pattern in Fig. 4d). Given that atmospheric air was used as an oxidant, this species likely originated from the reaction between Ba oxides migrated from the decomposed electrolyte and CO_2 from the air.

In the PBSCF area, SAED showed mostly retained PBSCF diffraction patterns (Fig. 4a, compare with the simulated SAED pattern in Fig. 4b); however, some extra diffraction peaks appeared at 4.5 Å and 3.4 Å, which can be attributable to $BaCO_3$. Additionally, extra diffraction peaks observed at larger angles (smaller *d*-spacings) at 3.1 Å, 1.8 Å, and 1.5 Å, can be attributed to BaO phases. Although slight degradation of the air electrode was observed, its impact on performance degradation appears minimal, as will be discussed in Section 3.4, which deals with the protective barrier layer approach.

In contrast, the SAED of the BCZYYb electrolyte shows a much more complex diffraction pattern compared to that of the air electrode region (Fig. 4e). A ring-like pattern indicates the development of much smaller polycrystalline grains associated with decomposed phases. The diffraction peak at 3.65 Å is attributable to $BaCrO_4$, Cr_2O_3, and/or $BaCO_3$ species. The peaks at 2.68 Å, 2.12 Å, 2.06 Å, and 1.73 Å are attributable to BaO and/or several different Ce–Zr-oxide phases. These lead to the conclusion that the decomposed electrolyte is composed of a Ba-rich region of $BaCO_3$ and BaO, with a small amount of $BaCrO_4$ and several different Ce–Zr-oxide species. Also, a significant depletion of Ba in the electrolyte phase suggests that the $BaCO_3$ phase (Position 2 in Fig. 3) is a segregated species resulting from the electrolyte decomposition.

The formation of an insulating $BaCO_3$ phase at the interface (Position 2) and the decomposition of the electrolyte (Position 4) likely contributed to the cell failure. Once the electrolyte decomposition and $BaCO_3$ formation extend horizontally across the interface, they can lead to a total blockage of charge carriers, resulting in the abrupt voltage drop observed in Fig. 1d. This degradation phenomenon in PCFCs has not been previously documented and may present a significant challenge for the commercialization of these cells.

3.4. Protective barrier layer for improving stability

Our findings indicated that cell degradation commences at the air electrode/electrolyte interface upon exposure to gaseous Cr-species, damaging the Ba-containing electrolyte (BCZYYb4411) and causing the migration of Ba, which forms a secondary $BaCO_3$ phase with CO_2. Therefore, shielding the electrolyte from exposure to gaseous species could improve PCFC stability. As PBSCF exhibited better stability than BCZYYb4411, a dense and thin interlayer of PBSCF was deposited at the interface using pulsed laser deposition. PBSCF, being a triple-conducting oxide

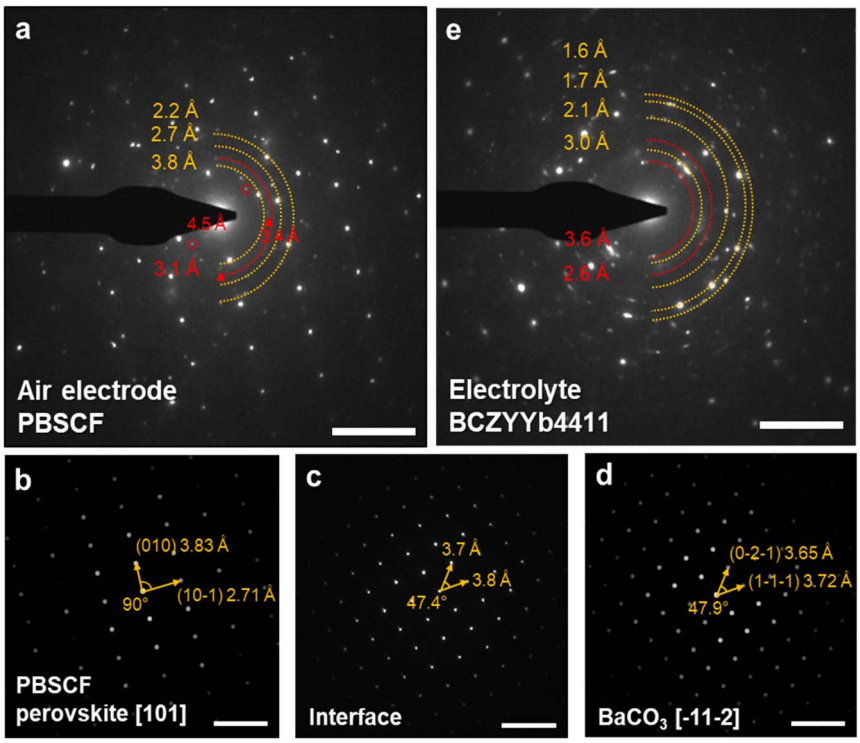

Fig. 4 Selected area electron diffraction (SAED) patterns acquired from the air electrode, interface, and electrolyte regions. (a) SAED pattern of the air electrode PBSCF. (b) Simulated perovskite PBSCF [101] pattern. The marked values are theoretical values. Extra diffraction peaks, corresponding to polycrystalline perovskite PBSCF, are indicated by yellow dashed half-circles. Other prominent diffraction peaks that do not correspond to the perovskite PBSCF are highlighted with red dashed half-circles (3.1 Å), small circles (4.5 Å), and triangles (3.4 Å). (c) SAED pattern taken at the interface, indexed to the $BaCO_3$ phase. The noted numbers are measured values. (d) Simulated $BaCO_3$ [−11−2] diffraction pattern. The marked values are theoretical values. (e) SAED pattern taken from the electrolyte, showing highly developed ring-line polycrystalline diffraction patterns. Polycrystalline rings associated with the BCZYYb4411 perovskite phase are marked with yellow dashed half-circles, while other diffraction rings not corresponding to BCZYYb4411 are marked with red dashed half-circles. Scale bar: 5 nm^{-1}. See Fig. S10† for the exact positions of SAED acquisitions.

capable of conducting protons, serves as an effective dense protective barrier layer.[4,34]

A dense and uniform PBSCF layer, 100 nm thick, was introduced (Fig. S11†) at the interface, and the modified cell was tested under the same conditions as the reference PCFCs shown in Fig. 1. As anticipated, the PCFC with the 100 nm PBSCF interlayer showed significantly enhanced stability under the same ~20 h operation period (Fig. S11d–g†), demonstrating that shielding the electrolyte from gaseous Cr species and CO_2 is crucial for improving stability. STEM-EDS images of the 100 nm interlayer-protected cell after ~20 h of operation—matching the operational timeframe of the reference cell in Fig. 1d—showed no phase decomposition or secondary phase, $BaCO_3$, formation. The compositional stoichiometry of the electrolyte was well maintained, with Cr content in the electrolyte below the detection limit. Post-20 h operation XRD analysis of the cell revealed no signs of degradation in either the electrolyte or the air electrode (Fig. S11h and i†). Notably, while the interlayer protected the electrolyte, it also prevented degradation of the air electrode, suggesting that PBSCF degradation might also be influenced by interface degradation phenomena. The improved stability resulting from the insertion of the dense PBSCF interlayer affirmatively confirmed that the electrolyte at the interface is indeed the primary site of cell degradation. PBSCF, having greater stability than BCZYYb4411, effectively protected the electrolyte and significantly extended longevity of the cell. However, even with a 100 nm PBSCF interlayer, minor degradation was observed in specific regions after the 20 h test (upper left region of Fig. 5a), and a slight decrease in electrochemical performance was observed (Fig. S11e and f†). Although the interlayer substantially improved stability, a thickness of 100 nm might not be thick enough to fully protect the electrolyte from degradation.

Interlayers of 100, 300, and 500 nm thickness were applied to the cell and tested for 100 h (Fig. 5b–f). The initial performances of the cells were assessed, showing a slight decrease in peak power density with increasing interlayer thickness (Fig. 5c–f). Electrochemical impedance analyses, presented in Fig. S12,† indicated total resistances of 0.44, 0.43, 0.52, and 0.65 Ω cm^2 for the cell without a PBSCF interlayer and cells with 100 nm, 300 nm, and 500 nm PBSCF interlayers, respectively. Adding a 100 nm interlayer resulted in nearly identical impedance spectra to those of the cell without an interlayer, whereas adding 300 nm and 500 nm interlayers increased both ohmic and polarization impedances. Long-term tests demonstrated remarkably improved stability (Fig. 5b). Linear-extrapolated

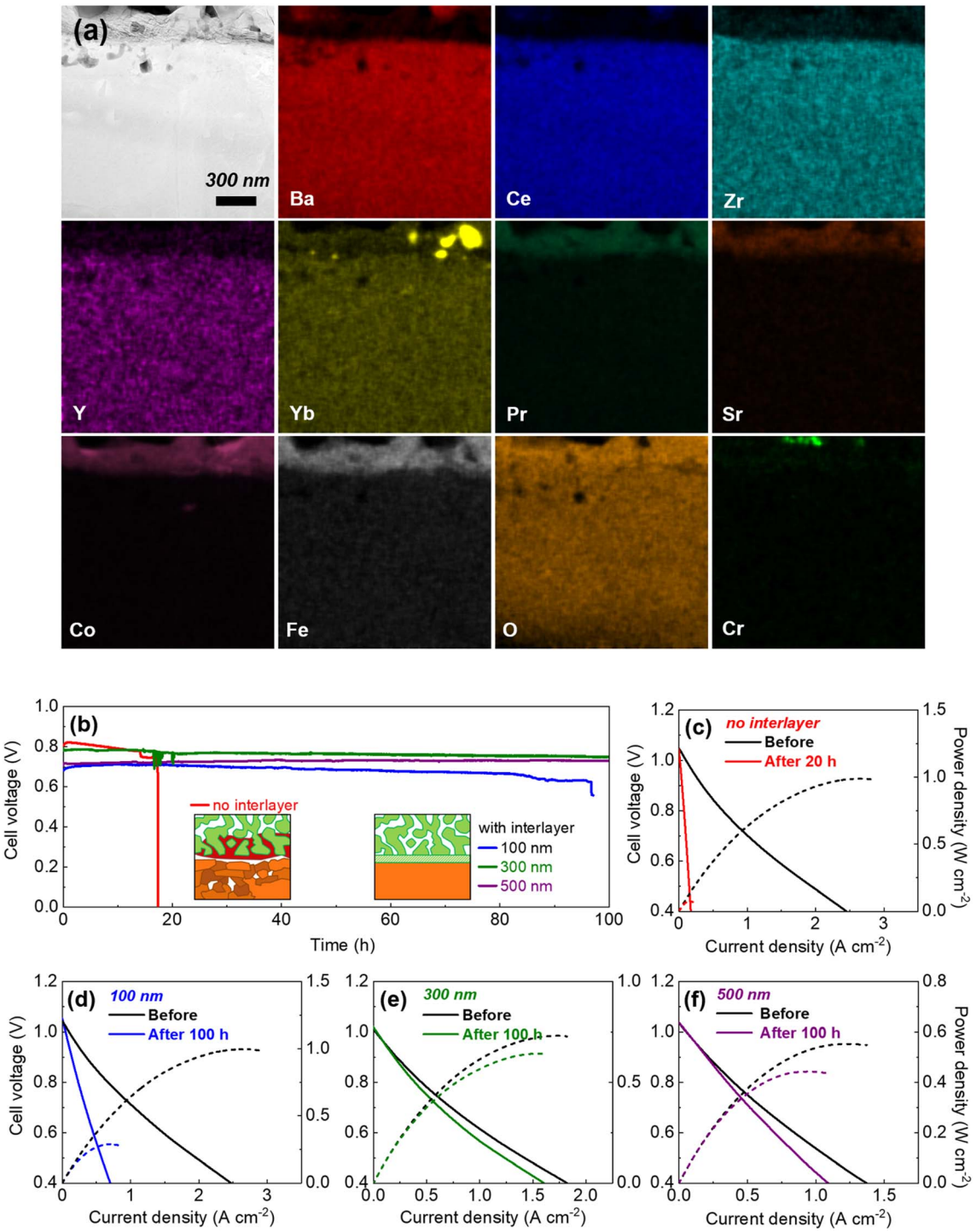

Fig. 5 The effect of a protective barrier layer on improving stability. (a) HAADF-STEM image and EDS mapping images of the constituent elements for the 100 nm PBSCF interlayer applied cell after a 20 h cell test. Quantitative element mapping (Q_{map}) was applied for Cr. (b) Galvanostatic test at 600 °C and a current density of 0.5 A cm^{-2} under fuel cell operation of the PCFC without a PBSCF interlayer and cells with dense PBSCF interlayers with thicknesses of 100 nm, 300 nm, and 500 nm. Inset: a schematic illustration describing the stability behavior of PCFCs with and without a protective barrier layer (c–f) *I–V–P* characteristics of the corresponding cells before and after the galvanostatic tests.

degradation rates were 428%, 93.9%, 40.8%, and 0% kh^{-1} for the cell without a PBSCF interlayer and cells with 100 nm, 300 nm, and 500 nm PBSCF interlayers, respectively. Similar to the reference cell, the 100 nm interlayer cell suffered an abrupt voltage drop near the end of the 100 h test. The HAADF-STEM and EDS mapping images (Fig. S13†) clearly depict the decomposition of the electrolyte layer and the formation of a Ba-rich secondary phase, presumably $BaCO_3$, filling the pores at

the interface of the cathode—demonstrating that similar degradation prevailed also with a 100 nm interlayer added cell. The 500 nm interlayer cell showed no noticeable voltage drop during the long-term test, which is the best stability reported for PCFCs operated under realistic conditions.[31,32] *I–V–P* curves and EIS spectra measured before and after the long-term test exhibited the same trend: the thicker the interlayer, the greater the stability. However, even the *I–V–P* curve for the 500 nm sample showed performance degradation after a 100 h test (Fig. 5f). Although the degradation of PBSCF was not as severe as BCZYYb4411, we still observed slight degradation of the PBSCF. Therefore, improving the stability of the air electrode still remains an ongoing challenge[32,35] as well as improvements to the protective barrier layer.

3.5. Further discussion on degradation of PCFCs under realistic operating conditions

Our observations clearly highlight the critical role of volatile Cr species in the degradation of PCFCs, especially at the air electrode/electrolyte interface. Various control tests confirmed that the Ba-containing electrolyte, BCZYYb4411, readily formed secondary phases with volatile Cr species, even at temperatures as low as 600 °C. Detailed TEM studies revealed severe decomposition of the electrolyte with significant Ba deficiency, leading to the formation of $BaCO_3$, $BaCrO_4$, and possibly BaO. Notably, significant degradation was observed only at the air electrode/electrolyte interface, suggesting the importance of electrochemical reactions or interactions between the air electrode and electrolyte materials.

Another important observation concerns the unexpected formation of large amounts of $BaCO_3$, despite its thermodynamic driving force for formation being significantly smaller than that for $BaCrO_4$ (Fig. S6†). Control tests confirmed that $BaCO_3$ does not readily form from the reaction between CO_2 and BCZYYb4411 (Fig. S1 and S4c†). These findings lead to the conclusion that an electrochemical reaction and/or exposure to Cr are crucial for the cell degradation, even considering the excessive formation of $BaCO_3$ at the interface.

The effectiveness of the protective barrier layer, as well as the observed thickness dependence, further confirms that exposure of the BCZYYb4411 electrolyte to volatile Cr and CO_2 species is the primary degradation mechanism. However, degradation was still observed in the PBSCF material and thus might have contributed to the observed cell degradation. Further improvements in barrier layer materials and air electrodes are necessary to enhance durability under realistic operating conditions.

The degradation mechanism is likely initiated by volatile Cr species interacting with the Ba-containing electrolyte at the interface, leading to the formation of insulating secondary phases. Accumulation of these insulating phases—primarily $BaCO_3$ and decomposed electrolyte—gradually lowers the cell performance by obstructing the electrochemically active interface, eventually causing sudden cell failure once complete obstruction occurs. However, this proposed mechanism is based only on post-mortem analyses and control tests. More detailed studies—ideally employing *in situ* techniques—are required to fully elucidate the exact degradation mechanism.

The observed degradation mechanism in PCFCs shows a clear difference from the Cr poisoning phenomena observed in SOFCs. In SOFCs, chromium poisoning is well-documented: it occurs as Cr_2O_3 or $(Cr,Mn)_3O_4$ segregation at the cathode–electrolyte interface in cells using $(La,Sr)MnO_3$ cathodes, obstructing ionic transport, or as $SrCrO_4$ formation on the cathode surface with $(La,Sr)(Co,Fe)O_3$ cathodes, leading to reduced surface active sites.[28,36–38] These phenomena decrease cell performance by limiting the number of ionic pathways or surface active sites and represent a steady and slow process. In contrast, we observed a different degradation mechanism leading to a sudden performance drop in PCFCs. We found that the Ba-containing electrolyte reacts with volatile Cr species, initiating rapid degradation at the air electrode/electrolyte interface and the formation of insulating secondary phases. Complete obstruction of the interface by these insulating phases results in sudden cell failure. As the cell failed within 20 h of operation, this degradation rate is significantly faster than that in conventional SOFCs.

We propose three main criteria for the protective barrier layer in protonic ceramic cells: (i) sufficient density to prevent gas impurities from reaching the electrolyte, (ii) stability in the presence of Cr, CO_2, and H_2O, while being compatible with the electrolyte and air electrode, and (iii) reasonable proton conductivity.

4. Conclusions

We observed severe degradation and phase decomposition in PCFCs under realistic operating conditions containing gaseous Cr species and CO_2. The degradation mechanism involves the formation of $BaCrO_4$, electrolyte decomposition, and segregation of $BaCO_3$ at the air electrode/electrolyte interface, which leads to drastic cell failure. Implementing a dense protective barrier layer composed of PBSCF at the air electrode/electrolyte interface can effectively shield the electrolyte from degradation. This study highlights the critical need to address Cr and CO_2 poisoning in PCFCs and protonic ceramic electrolyte cells (PCECs). Future strategies should focus on enhancing protective barrier layers, developing stable air electrode and electrolyte materials, and minimizing Cr evaporation from interconnects to foster the industrial relevance of PCFCs/PCECs.

Data availability

Data for this article, including electron microscopy images, electrochemical data, and XRD spectra, are available on Zenodo at **https://doi.org/10.5281/zenodo.13788333**.

Author contributions

Ms Yeji Lim: investigation, writing – original draft. Mr Jong Heon Chong: investigation, revising draft. Dr Puspendu Guha: investigation, visualization. Mr Wan-Jae Lee: investigation. Mr Inhyeok Cho: investigation. Dr Seol Hee Oh: methodology. Mr

Junseok Kim: investigation. Dr Kyung Joong Yoon: funding acquisition, supervision. Dr Ji-Won Son: methodology. Dr Jong-Ho Lee: supervision. Prof. Sihyuk Choi: investigation, methodology. Dr Deok-Hwang Kwon: investigation, methodology. Dr Ho-Il Ji: conceptualization, supervision, writing – review & editing. Dr Sungeun Yang: conceptualization, investigation, funding acquisition, supervision, writing – review & editing.

Conflicts of interest

There are no conflicts to declare.

Acknowledgements

This work was supported by the Nano Material Technology Development Program through the National Research Foundation of Korea (NRF) funded by the Ministry of Science and ICT (NRF-2022M3H4A1A04085315), and the National Research Council of Science & Technology (NST) grant by the Korea government (MSIT) (No. GTL24051-500).

Notes and references

1 R. Murphy, Y. C. Zhou, L. Zhang, L. Soule, W. L. Zhang, Y. Chen and M. L. Liu, *Adv. Funct. Mater.*, 2020, **30**, 2002265.
2 Z. Y. Luo, Y. C. Zhou, X. Y. Hu, N. Kane, T. T. Li, W. L. Zhang, Z. J. Liu, Y. Ding, Y. Liu and M. L. Liu, *Energy Environ. Sci.*, 2022, **15**, 2992–3003.
3 D. L. Han, X. Liu, T. S. Bjorheim and T. Uda, *Adv. Energy Mater.*, 2021, **11**, 2003149.
4 S. Choi, C. J. Kucharczyk, Y. G. Liang, X. H. Zhang, I. Takeuchi, H. I. Ji and S. M. Haile, *Nat. Energy*, 2018, **3**, 202–210.
5 H. Ding, W. Wu, C. Jiang, Y. Ding, W. Bian, B. Hu, P. Singh, C. J. Orme, L. Wang, Y. Zhang and D. Ding, *Nat. Commun.*, 2020, **11**, 1907.
6 F. He, S. Liu, T. Wu, M. T. Yang, W. H. Li, G. M. Yang, F. Zhu, H. Zhang, K. Pei, Y. Chen, W. Zhou and Z. P. Shao, *Adv. Funct. Mater.*, 2022, **32**, 2206756.
7 M. Z. Liang, F. He, C. Zhou, Y. B. Chen, R. Ran, G. M. Yang, W. Zhou and Z. P. Shao, *Chem. Eng. J.*, 2021, **420**, 127717.
8 Y. C. Zhou, E. Z. Liu, Y. Chen, Y. C. Liu, L. Zhang, W. L. Zhang, Z. Y. Luo, N. Kane, B. Zhao, L. Soule, Y. H. Niu, Y. Ding, H. P. Ding, D. Ding and M. L. Liu, *ACS Energy Lett.*, 2021, **6**, 1511–1520.
9 N. Wang, C. M. Tang, L. Du, R. J. Zhu, L. X. Xing, Z. Q. Song, B. Y. Yuan, L. Zhao, Y. Aoki and S. Y. Ye, *Adv. Energy Mater.*, 2022, **12**, 2201882.
10 K. Park, H. Bae, H. K. Kim, I. G. Choi, M. Jo, G. M. Park, M. Asif, A. Bhardwaj, K. S. Lee, Y. C. Kim, S. J. Song, E. D. Wachsman and J. Y. Park, *Adv. Energy Mater.*, 2023, **13**, 2202999.
11 Y. C. Zhou, W. L. Zhang, N. Kane, Z. Y. Luo, K. Pei, K. Sasaki, Y. M. Choi, Y. Chen, D. Ding and M. L. Liu, *Adv. Funct. Mater.*, 2021, **31**, 2105386.
12 H. An, S. Im, J. Kim, B. K. Kim, J. W. Son, K. J. Yoon, H. Kim, S. Yang, H. Kang, J. H. Lee and H. I. Ji, *ACS Energy Lett.*, 2022, **7**, 4036–4044.
13 H. An, H.-W. Lee, B.-K. Kim, J.-W. Son, K. J. Yoon, H. Kim, D. Shin, H.-I. Ji and J.-H. Lee, *Nat. Energy*, 2018, **3**, 870–875.
14 C. Duan, J. Tong, M. Shang, S. Nikodemski, M. Sanders, S. Ricote, A. Almansoori and R. O'Hayre, *Science*, 2015, **349**, 1321–1326.
15 M. Choi, J. Paik, D. Kim, D. Woo, J. Lee, S. J. Kim, J. Lee and W. Lee, *Energy Environ. Sci.*, 2021, **14**, 6476–6483.
16 D. Kim, K. T. Bae, K. J. Kim, H.-N. Im, S. Jang, S. Oh, S. W. Lee, T. H. Shin and K. T. Lee, *ACS Energy Lett.*, 2022, **7**, 2393–2400.
17 K. Bae, D. H. Kim, H. J. Choi, J. W. Son and J. H. Shim, *Adv. Energy Mater.*, 2018, **8**, 1801315.
18 F. Liu, H. Deng, D. Diercks, P. Kumar, M. H. A. Jabbar, C. Gumeci, Y. Furuya, N. Dale, T. Oku, M. Usuda, P. Kazempoor, L. Fang, D. Chen, B. Liu and C. Duan, *Nat. Energy*, 2023, **8**, 1145–1157.
19 W. Bian, W. Wu, B. Wang, W. Tang, M. Zhou, C. Jin, H. Ding, W. Fan, Y. Dong, J. Li and D. Ding, *Nature*, 2022, **604**, 479–485.
20 C. Duan, R. J. Kee, H. Zhu, C. Karakaya, Y. Chen, S. Ricote, A. Jarry, E. J. Crumlin, D. Hook, R. Braun, N. P. Sullivan and R. O'Hayre, *Nature*, 2018, **557**, 217–222.
21 S. Choi, T. C. Davenport and S. M. Haile, *Energy Environ. Sci.*, 2019, **12**, 206–215.
22 C. C. Duan, R. Kee, H. Y. Zhu, N. Sullivan, L. Z. Zhu, L. Z. Bian, D. Jennings and R. O'Hayre, *Nat. Energy*, 2019, **4**, 230–240.
23 J. W. Mao, E. H. Wang, H. W. Wang, M. G. Ouyang, Y. P. Chen, H. R. Hu, L. G. Lu, D. S. Ren and Y. D. Liu, *Renewable Sustainable Energy Rev.*, 2023, **185**, 113597.
24 E. J. Opila, D. L. Myers, N. S. Jacobson, I. M. Nielsen, D. F. Johnson, J. K. Olminsky and M. D. Allendorf, *J. Phys. Chem. A*, 2007, **111**, 1971–1980.
25 B. Talic, E. Stefan and Y. Larring, in *High-temperature Electrolysis*, ed. W. Sitte and R. Merkle, IOP Publishing, London, UK, 2023, ch. 5, pp. 5-1–5-21.
26 H. Yokokawa, T. Horita, N. Sakai, K. Yamaji, M. E. Brito, Y. P. Xiong and H. Kishimoto, *Solid State Ionics*, 2006, **177**, 3193–3198.
27 K. Suksumrit, S. Kleiber and S. Lux, *Energies*, 2023, **16**(7), 2973.
28 R. F. Wang, Z. H. Sun, Y. C. Lu, S. Gopalan, S. N. Basu and U. B. Pal, *J. Power Sources*, 2020, **476**, 228743.
29 S. Taniguchi, M. Kadowaki, T. Yasuo, Y. Akiyama, Y. Itoh, Y. Miyake and K. Nishio, *Denki Kagaku*, 1996, **64**, 568–574.
30 L. Zhao, D. Ding, L. Zhang, L. Gui, Z. Wang, Y. Wan, R. Wang, Y. Ling and B. He, *Int. J. Hydrogen Energy*, 2014, **39**, 18379–18384.
31 L. Q. Le, C. Meisel, C. H. Hernandez, J. Huang, Y. Kim, R. O'Hayre and N. P. Sullivan, *J. Power Sources*, 2022, **537**, 231356.
32 H. Zhang, K. Xu, F. He, Y. C. Zhou, K. Sasaki, B. T. Zhao, Y. Choi, M. L. Liu and Y. Chen, *Adv. Energy Mater.*, 2022, **12**, 2200761.

33 K. Pei, Y. Zhou, K. Xu, H. Zhang, Y. Ding, B. Zhao, W. Yuan, K. Sasaki, Y. Choi, Y. Chen and M. Liu, *Nat. Commun.*, 2022, **13**, 2207.
34 S. Im, M. A. Berk, S. Yang, B. K. Kim, K. J. Yoon, J. W. Son, J. H. Lee and H. I. Ji, *J. Mater. Chem. A*, 2022, **10**, 16127–16136.
35 M. Choi, S. J. Kim and W. Lee, *Ceram. Int.*, 2021, **47**, 7790–7797.
36 T. Horita, *Ceram. Int.*, 2021, **47**, 7293–7306.
37 X. Chen, L. Zhang, E. Liu and S. P. Jiang, *Int. J. Hydrogen Energy*, 2011, **36**, 805–821.
38 B. Wei, K. Chen, L. Zhao, Z. Lu and S. P. Jiang, *Phys. Chem. Chem. Phys.*, 2015, **17**, 1601–1609.